Journal of Materials Chemistry

Cite this: *J. Mater. Chem.*, 2012, **22**, 13110

www.rsc.org/materials

PAPER

Hybrid polythiophene–clay exfoliated nanocomposites for ultracapacitor devices

David Aradilla,[ab] Denise Azambuja,*[c] Francesc Estrany,[bd] Maria T. Casas,[a] Carlos A. Ferreira[e] and Carlos Alemán*[ab]

Received 5th March 2012, Accepted 30th April 2012
DOI: 10.1039/c2jm31372c

Exfoliated nanocomposites of poly(3,4-ethylenedioxythiophene) (PEDOT) and montmorillonite (MMT) have been prepared by *in situ* anodic polymerization, concentrations of clay ranging from 5% w/w to 50% w/w being included in the aqueous polymerization medium. The morphology, electrical conductivity, adherence, thermal stability, charge storage, specific capacitance, electrostability, doping level and band gap have been determined for the different PEDOT–MMT nanocomposites and compared with those of pristine PEDOT. Many of these properties have been found to depend on both the concentration of clay and the thickness (micrometric or nanometric) of the generated films. Types I and II ultracapacitors have been fabricated using nanometric and micrometric films of PEDOT and PEDOT–MMT. The properties of such devices have been characterized and compared with those reported in the literature for ultracapacitors fabricated using nanocomposites of PEDOT and other inorganic materials. Both nanometric and micrometric type II ultracapacitors, which correspond to an asymmetric configuration of PEDOT and PEDOT–MMT films, have been found to present the better properties (*e.g.* the specific capacitance for nanometric and micrometric devices is 429 and 116 F g^{-1}, respectively), evidencing the favorable effect of the clay. Finally, the effects of the electrochemical degradation on the ultracapacitors have been rationalized using electrochemical impedance spectroscopy.

Introduction

Among polythiophene derivatives, poly(3,4-ethylenedioxythiophene) (PEDOT; Scheme 1) has attracted much attention because of its many advantageous properties such as high electrical conductivity (up to 500 S cm^{-1}) and transparency in the visible range, excellent thermal and structural stability, suitable morphology and fast doping–undoping mechanism.[1–5] Many of the properties of PEDOT, which was developed at the end of the eighties in Germany,[6] are due to the fact that in the 3,4-ethylenedioxythiophene (EDOT) monomer the positions 3 and 4 of the thiophene ring are protected by the dioxane ring.[1,7–11] PEDOT has already found useful applications as antistatic film coating,[12–14] electrochromic windows,[15] hole-injection material in organic light emitting diodes (LEDs),[16] ultracapacitors,[17–19] and lithium ion batteries.[2,20]

On the other hand, the development of conducting polymer–clay nanocomposites is receiving increasing interest due to their

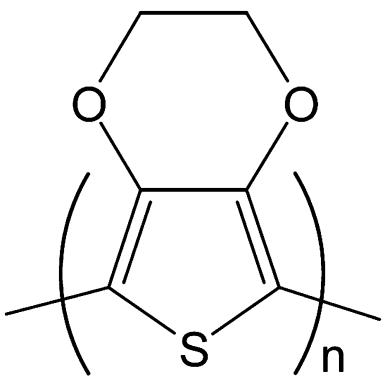

PEDOT

Scheme 1

[a]*Departament d'Enginyeria Química, E. T. S. d'Enginyers Industrials, Universitat Politècnica de Catalunya, Diagonal 647, 08028 Barcelona, Spain. E-mail: carlos.aleman@upc.edu*
[b]*Center for Research in Nano-Engineering, Universitat Politècnica de Catalunya, Campus Sud, Edifici C', C/Pasqual i Vila s/n, Barcelona E-08028, Spain*
[c]*Institute of Chemistry, Federal University of Rio Grande do Sul, Av. Bento Gonçalves 9500, CEP 91501-970 Porto Alegre, RS Brazil. E-mail: denise@iq.ufrgs.br*
[d]*Unitat de Química Industrial, Escola Universitària d'Enginyeria Tècnica Industrial de Barcelona, Universitat Politècnica de Catalunya, Comte d'Urgell 187, 08036 Barcelona, Spain*
[e]*Universidade Federal do Rio Grande do Sul, DEMAT, Av. Bento Gonçalves, 9500 - setor 4- prédio 74, Cep. 91501-970 Porto Alegre, RS – Brazil*

important technological applications. Specifically, hybrid materials formed by the combination of polyaniline or polypyrrole with clay minerals structured at the nanoscale level have been used as electrochemical sensors[21,22] and anticorrosive coatings.[23–25] The main benefit induced by the incorporation of the clay was the improvement of the thermal stability, which was found to be higher for the polyaniline–clay[26–28] and polypyrrole–clay[29,30] nanocomposites than for the pristine conducting polymers.

Some hybrid PEDOT–clay nanocomposites based on montmorillonite (MMT), which is a smectite group mineral clay that belongs to the general family of 2 : 1 layered silicates, have been reported in the last few years.[31–34] Since exfoliated conducting polymer–clay nanocomposites usually have better properties (*e.g.* stiffness, strength and barrier property) than the intercalative ones, it is rationalized that the higher the degree of exfoliation, the greater the enhancement of these properties.[35] Unfortunately, PEDOT–MMT nanocomposites prepared by Leta *et al.*[31] and Rajapakse *et al.*[32] showed an intercalative structure rather than the more desirable exfoliated organization. Han and Lu[33] reported exfoliated PEDOT–MMT nanocomposites that were obtained by *in situ* polymerization in aqueous media using modified clays. Although the thermal stability of the nanocomposite was better than that of pristine PEDOT, its electrical conductivity was very low (10^{-7} to 10^{-2} S cm^{-1}).[33] More recently, we reported an *in situ* electropolymerization procedure to prepare exfoliated PEDOT–MMT nanocomposites using non-modified clays, the electrical conductivities of the produced hybrid materials ranging from 1 to 4 S cm^{-1}.[34] Differences in the electrical conductivity of these two PEDOT–MMT nanocomposites should be attributed to both the efficacy of the dopant agent (*i.e.* the oxidant power of lithium perchlorate[34] is higher than that of the organic dopant agents used in ref. 33) and the molecular length of PEDOT chains, which is larger when prepared electrochemically. However, in both cases exfoliated composites were prepared using relatively low clay concentrations ($\leq$10% w/w).[33,34]

Electrochemical capacitors are charge storage devices of high power and energy density, which exhibit reversibility and long cycle life. If the capacitance in these devices is stored as a build-up of charge in the electrical double-layer in the solution interface, the capacitor is called an electric double layer capacitor. However, if the capacitance is stored in the bulk of the electrode material in response to a redox reaction, the capacitor is denoted ultracapacitor or pseudocapacitor. Unlike batteries, electrochemical capacitors store their energy in an electrostatic field rather than in chemical form.[36–38] Electrode materials for ultracapacitors mainly include carbon, transition-metal oxides, and conducting polymers.[39–41] In a recent review Snook *et al.*[41] focused on composites based on conducting polymers that are used for electrochemical capacitor devices. Despite this, the exploration, improvement and discovery of new electrode materials to achieve ultracapacitors with better electrochemical properties remains a challenge.

In a recent study we examined the behavior as ultracapacitors of electrodes formed by alternated layers of PEDOT and poly(N-methylpyrrole) (ml-PEDOT/PNMPy).[18] The specific capacitance (SC) for a symmetric assembly of two identical multilayered ml-PEDOT/PNMPy electrodes (SC = 90 F g^{-1}) was found to be significantly higher than that obtained for two PEDOT electrodes (SC = 41 F g^{-1}). These values were considerably lower than those reported for ultracapacitors fabricated using nanocomposites of PEDOT and inorganic materials (*e.g.* MoO_3, RuO_2, carbon nanotubes, MnO_2, and $NiFe_2O_4$), for which the SC ranged from 153 to 375 F g^{-1}.[42–48] However, to the best of our knowledge there is no investigation about the performance of PEDOT–MMT nanocomposites as ultracapacitors.

Both the inexistence of exfoliated PEDOT–MMT nanocomposites with high concentrations of clay and the lack of information about the performance of these hybrid materials as ultracapacitors have motivated the current study. Specifically, this work reports the preparation and characterization of exfoliated PEDOT–MMT nanocomposites obtained using MMT concentrations in the monomer solution that ranged from 5% to 50% w/w (dry weight). After this, the morphology and topography, electrical conductivity, adherence, thermal stability, charge store ability, electrochemical stability, specific capacitance and doping level of the nanocomposites have been investigated and compared with the properties of pristine PEDOT. Next, we have examined the performance of PEDOT–MMT nanocomposites to be used as ultracapacitors of both type I (*i.e.* symmetric systems using the same nanocomposite for the two electrodes) and type II (*i.e.* asymmetric based electrodes made of PEDOT and PEDOT–MMT). Finally, electrochemical impedance spectroscopy (EIS) studies have been performed on selected ultracapacitors to examine the circuit elements that explain their successful behavior as well as to compare the corresponding physical and electrochemical parameters.

Methods

Materials. 3,4-Ethylenedioxythiophene (EDOT) monomer and MMT (bentonite) were purchased from Aldrich and used as received. Anhydrous $LiClO_4$, analytical from Aldrich, analytical reagent grade, was stored in an oven at 80 °C before use in the electrochemical trials.

Synthesis. The synthetic process used to prepare both PEDOT and PEDOT–MMT was identical to that reported in our previous work[34] and, therefore, here we only provide a brief summary. The conducting polymer and the nanocomposite were produced by chronoamperometry (CA) under a constant potential of 1.10 V with an Autolab PGSTAT302N (Ecochimie, The Netherlands) potentiostat/galvanostat equipped with GPES and FRA software and using a conventional three-electrode system. Steel AISI 316 sheets of 4 cm^2 were used as electrodes. The generation medium consisted of a 10 mM EDOT solution in distilled water containing 0.1 M $LiClO_4$ as supporting electrolyte. Both micrometric and nanometric films of all the investigated materials were prepared considering polymerization times (τ) of 300 s and 30 s, respectively. The concentration of MMT in the generation medium, which is referred to that of the EDOT monomer, ranged from 5% to 50% w/w (dry weight). Before the addition of MMT to the monomer solution, the clay was exfoliated in deionized water at neutral pH, being sonicated 10 min with an ultrasonic generator. The resulting solution was stirred for 1 day using a magnetic stirrer. Next, the generation medium

and the exfoliated MMT solution were mixed and stirred for 20 h in a frozen environment (ice).

FTIR spectroscopy. FTIR spectra were recorded on a FTIR 4100 Jasco spectrophotometer with a resolution of 4 cm^{-1} in the absorbance mode. The samples were placed in an attenuated total reflection accessory with thermal control and a diamond crystal (Golden Gate Heated Single Reflection Diamond ATR).

Thickness. The thickness of the films was determined through gravimetric, electrochemical and structural measurements. Gravimetric estimations were obtained through the mass of polymer deposited in the electrode, which was obtained using a Sartorious ultra-microbalance, the surface of polymerization (*i.e.* the surface of the electrode, 4 cm^2) and the density of the materials. The latter was determined by the flotation method from $CCl_4 + C_2H_5I$ mixtures. Electrochemical estimations of the thickness were obtained by determining the current productivity through the mass–charge ratio and, subsequently, the mass of polymer deposited in the electrode. The latter procedure was detailed in previous works.[49,50] Finally, the thicknesses of nanometric and micrometric films were also determined by scratch atomic force microscopy (AFM) and by cross-sectional scanning electron microscopy (SEM), respectively.

Transmission electron microscopy (TEM). The structure and distribution of the clay in nanocomposites was examined using a Phillips TECNAI 10 transmission electron microscope at an accelerating voltage of 100 kV. For this purpose, small strips of nanocomposites were removed from the electrodes with a razor blade and, according to the manufacturer's protocol, embedded in a low viscosity modified Spurr epoxy resin and cured at 60 °C for 24 h. Ultra-thin sections (less than 100 nm) of these samples were cut at room temperature using a Sorvall Porter-Blum microtome. Finally, the sections were placed on carbon coated copper grids. Bright field micrographs were taken with a SIS Mega View II digital camera.

Scanning electron microscopy (SEM) and energy dispersive X-ray (EDX) spectroscopy. EDX spectroscopy and SEM studies were performed to examine the composition of the synthesized nanocomposites and to examine the effect of the clay on the surface morphology, respectively. Dried samples were placed in a Focussed Ion Beam Zeiss Neon 40 scanning electron microscope operating at 3 kV, equipped with an EDX spectroscopy system.

Atomic force microscopy (AFM). Topographic AFM images were obtained with a Molecular Imaging PicoSPM using a Nano-Scope IV controller in ambient conditions. The averaged RMS roughness (r) was determined using the statistical application of the Nanoscope software, which calculates the average considering all the values recorded in the topographic image with the exception of the maximum and the minimum. AFM measurements were performed on various parts of the films, which produced reproducible images similar to those displayed in this work.

Electrical conductivity and adherence. The electrical conductivity was determined using the sheet resistance method with a previously described procedure.[51]

Adherence measurements were based on the standard sello-tape test (TESA-4204 BDF), which consists of cutting the film into small squares, sticking the tape on it and then stripping it. The ratio between the number of adherent film squares remaining and their total number gives the percentage adherence.

Thermal analyses. The thermal stability was examined by thermogravimetric analysis (TGA) with a PerkinElmer TGA-6 thermobalance at a heating rate of 10 °C min^{-1} under a nitrogen atmosphere.

Electrochemistry. The electroactivity, which refers to the charge storage ability, and electrochemical stability (electrostability) were determined by cyclic voltammetry (CV) using a distilled water solution with 0.1 M $LiClO_4$. The initial and final potentials were −0.50 V, while the reversal potential was 1.00 V. The scan rate was 100 mV s^{-1} in all cases. The electroactivity increases with the similarity between the anodic and cathodic areas of the first control voltammograms, whereas the electrostability decreases with the oxidation and reduction areas of consecutive control voltammograms. Specifically, the loss of electrostability (LES, in %) was determined as:

$$\mathrm{LES} = \frac{\Delta Q}{Q_{\mathrm{II}}} \times 100 \quad (1)$$

where ΔQ is the difference of voltammetric charges (in C) between the second and the last cycle, and Q_{II} is the voltammetric charge corresponding to the second cycle. In this work, measures of LES refer to 100 consecutive oxidation–reduction cycles for both single electrode and two assembled electrodes (ultracapacitors) configurations unless a different number of cycles is explicitly specified (*i.e.* selected ultracapacitors have been also studied after 500 and 2000 consecutive oxidation–reduction cycles). Electrochemical estimation of the doping level (dl) was carried out using the following equation:

$$\mathrm{dl} = \frac{2Q_0}{Q_{\mathrm{D}} - Q_0} \times 100 \quad (2)$$

where Q_{D} is the total charge used for the nanocomposite deposition and Q_0 is total charge of oxidized species in the nanocomposite films.

The number of electrons consumed to incorporate a monomer into a polymer and to oxidize the resulting chain (n_{ox}) have been determined using a previously reported procedure.[52,53] For this purpose, the following equation has been used:

$$n_{\mathrm{ox}} = \frac{MQ_{\mathrm{pol}}}{FW_{\mathrm{ox}}(1 - W_{\mathrm{dop}})} \quad (3)$$

where M is the molar mass of EDOT, Q_{pol} is the polymerization charge consumed in each process (in millicoulombs per centimeter square) that was calculated on each chronoamperogram, F is the Faraday constant, W_{ox} is the film weight (in milligram per centimeter square) and W_{dop} is the mass of dopant per polymer unit of mass.

The SCs (in F g^{-1}) of PEDOT and the nanocomposites were determined by CV using the following equation:

$$\mathrm{SC} = \frac{Q}{\Delta Vm} \quad (4)$$

where Q is the voltammetric charge, which is determined by integrating either the oxidative or reductive parts of the cyclic voltammetry curve, ΔV is the potential window (in V), and m is the mass of polymer on the surface of the working electrode (in g).

Galvanostatic charge–discharge curves were used to evaluate the power density (P) and the maximum specific energy (E_{max}):

$$P = \Delta V \frac{I}{m} \quad (5)$$

$$E_{max} = \frac{SC V_{max}^2}{2m} \quad (6)$$

where ΔV is the difference between the potential at the beginning and at the end of the discharge, I is the applied current (1 mA) and m is the mass of active material in the electrodes, and V_{max} is the potential at the beginning of the discharge. Moreover, charge–discharge profiles were also used as an alternative method to measure the SC:

$$SC = \frac{i\Delta t}{\Delta V m} \quad (7)$$

where i is the current intensity and Δt is the time interval required for the change in voltage ΔV.

EIS measurements of different ultracapacitor configurations, which were prepared by assembling PEDOT and/or PEDOT–MMT films, were performed in potentiostatic mode at the open circuit potential (OCP) using an AUTOLAB PGSTAT 30/FRA 2 system. The amplitude of the EIS perturbation signal was 5 mV, and the studied frequency ranged from 10 kHz to 10 mHz. All experiments were carried out in a distilled water solution containing 0.1 M $LiClO_4$ at 25 °C.

The SC derived from EIS results was derived from the slope of the linear correlation between the imaginary impedance (Z_{im}, in Ω) and the reciprocal of the frequency (f, in Hz) at low frequencies, according to:

$$SC = -\frac{1}{2\pi f Z_{im} m} \quad (8)$$

Results and discussion

Preparation and characterization of PEDOT–MMT nanocomposites

PEDOT–MMT films were prepared by *in situ* anodic polymerization considering 5%, 10%, 20%, 30% and 50% w/w MMT in the generation media and $\tau = 300$ s and 30 s, respectively. In all cases the color of the micrometric ($\tau = 300$ s) and nanometric ($\tau = 30$ s) films was dark blue and blue sky, respectively, no difference being detected with respect to pristine PEDOT prepared using identical experimental conditions. However, the successful incorporation of the clay during the polymerization process was confirmed by FTIR and EDX spectroscopy. The FTIR spectra of all PEDOT–MMT nanocomposites (not displayed) showed the characteristic band of the Si–O stretching mode centered at 1044 cm^{-1} and the absorption bands centered at 524 and 467 cm^{-1}, which correspond to the Si–O–Al and Si–O–Si bending vibrations, respectively.[54] As expected, the spectra of PEDOT–MMT nanocomposites exhibited the characteristic bands of PEDOT in the range of 1052–837 cm^{-1}. On the other hand, qualitative composition analyses by EDX spectroscopy indicated that the concentration of MMT in the films, which was measured through the peaks of Al, Mg, Si and Na [*i.e.* the latter was the metallic counter-ion of the bentonite used in this work: $Na_x(Al_{4-x}Mg_x)Si_8O_2$], increases with its concentration in the generation medium.

The thickness of all the films was determined using gravimetric, electrochemical and SEM (micrometric)/AFM (nanometric) procedures (see Methods section for a description of each one). Table 1 compares the thickness of the films obtained for the different nanocomposites with those obtained for pristine PEDOT. The three methods are fully consistent, the thickness obtained for micrometric and nanometric films being ~1 μm and ~200 nm, respectively. Moreover, the thickness increases with the content of clay, even although this effect is more clear for nanometric than for micrometric films.

The round-like shape morphology of the MMT particles before exfoliation is displayed in Fig. 1a. The average diameter of these particles, which shows flake morphology, determined by SEM measurements is 8 ± 1 μm. The exfoliated distribution of the clay in micrometric nanocomposites with MMT 5% w/w and 10% w/w was demonstrated in our previous work.[34] In order to re-investigate this issue, TEM samples were cut perpendicular to the electrode surface. The MMT was found to be exfoliated into individual platelets within the PEDOT matrix in all the nanocomposites, this feature being clearly reflected in Fig. 1b for the nanometric systems with a clay concentration of 5% and 20% w/w, respectively.

Properties of the nanocomposites

Fig. 2a and b show SEM micrographs of nanometric PEDOT and PEDOT–MMT 5% w/w films, respectively. Although the agglomerates are slightly larger in the latter than in former, low

Table 1 Thickness of the pristine PEDOT and PEDOT–MMT nanocomposite films produced using polymerization times of 300 s and 30 s. The thickness was determined through gravimetric, electrochemical, SEM/AFM (micrometric/nanometric films) measurements

	Gravimetric		Electrochemical		SEM	AFM
System	300 s	30 s	300 s	30 s	300 s	30 s
PEDOT	0.91 μm	203 nm	1.06 μm	196 nm	0.84 μm	217 nm
PEDTOT-MMT 5%	1.07 μm	191 nm	1.16 μm	185 nm	1.19 μm	202 nm
PEDOT-MMT 10%	0.98 μm	208 nm	1.09 μm	204 nm	—	224 nm
PEDOT-MMT 20%	1.27 μm	229 nm	1.48 μm	227 nm	—	243 nm
PEDOT-MMT 50%	1.16 μm	237 nm	1.38 μm	216 nm	1.24 μm	251 nm

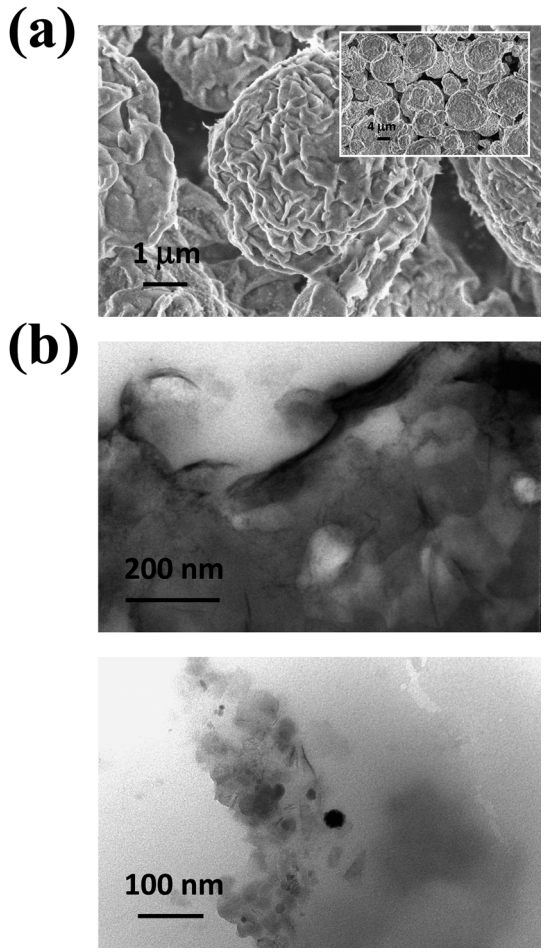

Fig. 1 (a) High- and low-resolution (inset) SEM micrographs of MMT particles before exfoliation. (b) TEM micrographs of nanometric PEDOT–MMT 5% w/w (upper) and PEDOT–MMT 20% w/w (lower).

concentrations of clay do not produce appreciable changes in the surface morphology. In spite of this, SEM micrographs of the internal side of the same PEDOT–MMT 5% w/w film shows the presence of granules, which are homogeneously distributed. This feature is also evidenced in the SEM micrograph displayed in

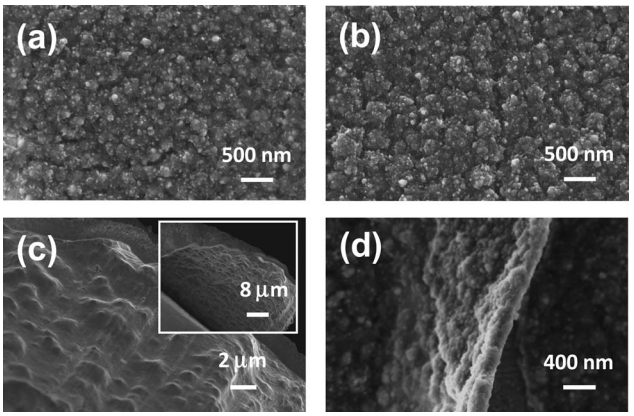

Fig. 2 SEM micrographs of nanometric (a) PEDOT and (b) PEDOT–MMT 5% w/w films. The internal side of the micrometric PEDOT–MMT 5% w/w film is displayed in (c) while (d) shows the cross-section of the nanometric PEDOT–MMT 5% w/w.

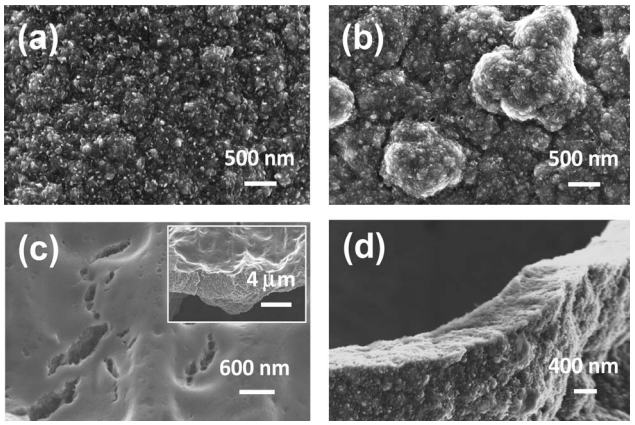

Fig. 3 SEM micrographs of micrometric (a) PEDOT and (b) PEDOT–MMT 20% w/w films. The internal side of the latter nanocomposite is displayed in (c) while (d) shows the cross-section of PEDOT.

Fig. 2c, which corresponds to the micrometric PEDOT–MMT 5% w/w film. These results suggest that when the concentration of MMT in the generation medium is very low with respect to that of EDOT monomer, the clay precipitates on the electrode provoking the presence of such granules. In contrast, large agglomerates appear in the surface of the nanocomposite when the MMT concentration is ≥20% w/w. This is evidenced in Fig. 3a and b, which compares the SEM micrographs of micrometric PEDOT and PEDOT–MMT 20% w/w films. Moreover,

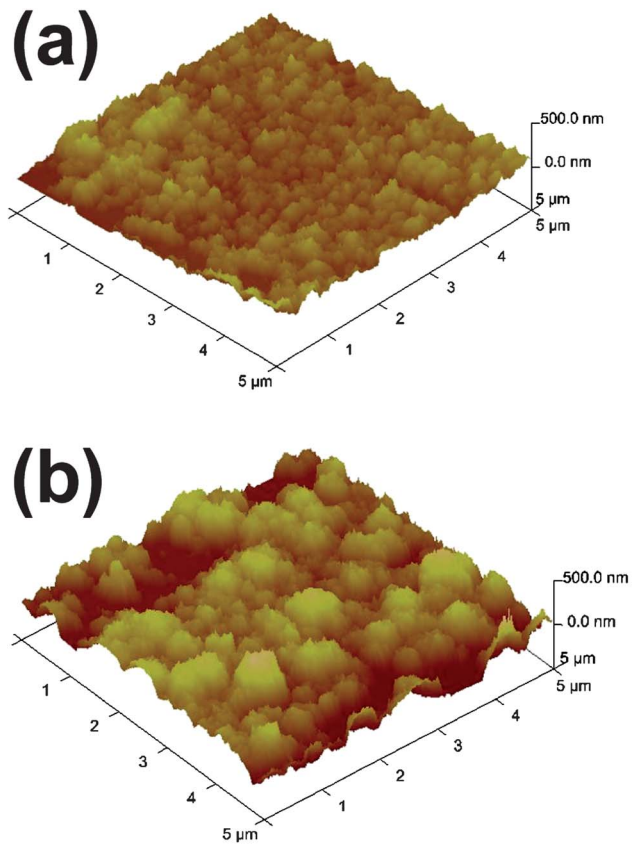

Fig. 4 3D AFM images illustrating the topographical changes induced by the incorporation of MMT ≥ 20% w/w. The images correspond to nanometric films of (a) PEDOT and (b) PEDOT–MMT 20% w/w.

these agglomerates alter the topography of the surface in both micrometric and nanometric films. Fig. 4 shows the AFM images of nanometric PEDOT and PEDOT–MMT 20% w/w films. As can be seen, PEDOT presents small clusters of aggregated molecules homogeneously distributed, this topography being consequence of the linear growing of polymer chains (*i.e.* molecules are exclusively formed by α–α linkages because the β-positions of the thiophene ring are occupied by the dioxane ring).[55] This topography becomes much less regular upon the incorporation of MMT 20% w/w, which promotes the formation of larger and higher aggregates. Interestingly, analysis of the internal sides of the films with a MMT concentration >10% w/w did not show granular structure (as was evidenced in Fig. 2c for the films with a lower concentration of MMT) but the presence of thin cracks (Fig. 3c). The latter should be attributed to a swelling effect due to the absorption of water from the medium. On the other hand, Fig. 2d and 3d show the cross-section of the nanometric PEDOT–MMT 5% w/w and micrometric PEDOT films, respectively, that were used to measure the thickness (~200 nm and ~1 μm, respectively).

The electrical conductivities measured at room temperature for micrometric PEDOT and PEDOT–MMT films are compared in Table 2. The effect of the exfoliated clay on the electrical conductivity of PEDOT (5.5 S cm^{-1}) is practically negligible for MMT concentrations ≤10 w/w while it drops one order of magnitude when the content of clay is >10% w/w. These results represent a very remarkable improvement with respect to those previously reported in the literature. Thus, the conductivity at room temperature reported for intercalated PEDOT–MMT was lower than 10^{-5} S cm^{-1} in all cases,[31,32] whereas that of the exfoliated nanocomposites prepared using organically modified MMT was around 10^{-8} S cm^{-1}.[33] In our previous study, we showed that the electrical conductivity of PEDOT decreased from 5.6 to 1.4 S cm^{-1} in 35 days, whereas that of PEDOT–MMT 5% w/w became practically negligible (<10^{-3} S cm^{-1}) after 17 days.[34] Analysis of the temporal evolution of the electrical conductivity for PEDOT–MMT 20% w/w indicated a decrease from 0.2 S cm^{-1} to 9 10^{-4} S cm^{-1} in 15 days, and a subsequent reduction to ~10^{-5} S cm^{-1} in 40 days, the latter value being retained by more than two months. These features indicate that, although the loss of electrical stability increases with the concentration of clay, this progressive reduction is only moderate. Furthermore, it is worth noting that, in spite of its poor electrical stability, the lower limit of the electrical conductivity reached for these nanocomposites is similar to the value reported for fresh samples of some polythiophene derivatives (~10^{-5} to 10^{-7} S cm^{-1}).[56–58]

Table 2 Electrical conductivity (κ, in S cm^{-1}) and adherence relative to PEDOT (in %) for micrometric films

	κ	Adherence
PEDOT	5.5	—
PEDOT–MMT 5% w/w	3.5	18
PEDOT–MMT 10% w/w	1.3	22
PEDOT–MMT 20% w/w	0.4	29
PEDOT–MMT 30% w/w	0.2	30
PEDOT–MMT 50% w/w	0.1	32

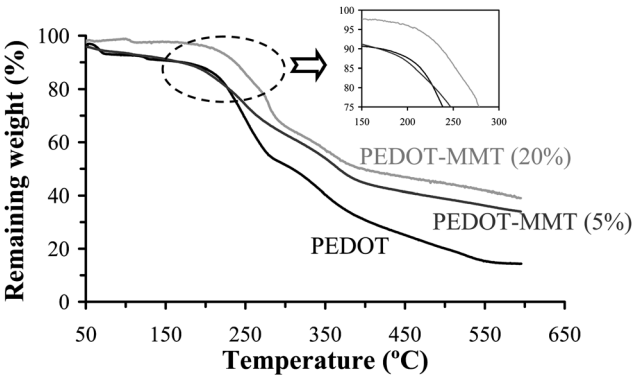

Fig. 5 Thermogravimetric curves of PEDOT, PEDOT–MMT 5% w/w and PEDOT–MMT 20% w/w. Details of the region encircled with a dashed line are provided in the inset.

The adherence was estimated using a normalized sellotape test, the resulting values relative to PEDOT being displayed in Table 2. The exfoliated clay improves the adherence of micrometric PEDOT films, this effect increasing moderately with the concentration of MMT. Accordingly, the measured adherence gain ranges from 18% (5% w/w) to 32% (50% w/w).

The thermal stability of clay-containing nanocomposites is typically higher than that of pristine polymers.[26–30] TGA curves for PEDOT and PEDOT–MT (both 5% and 20% w/w) are compared in Fig. 5. In all cases the thermal decomposition of the nanocomposites shifts towards higher temperatures than that of pristine PEDOT. Furthermore, the thermal stability increases moderately with the concentration of MMT. The weight loss at temperatures lower than 120 °C should be attributed to the evaporation of solvent (water). After this, a pronounced fall occurs between 200 °C and 300 °C, this process corresponding to the degradation of the polymer. More specifically, the thermal degradation of PEDOT, PEDOT–MMT 5% w/w and PEDOT–MMT 20% w/w occur at 228, 233 and 269 °C, respectively. The thermal decomposition of $LiClO_4$ occurs between 350 °C and 390 °C. Finally, the weight loss detected at temperatures ranging between 430 °C and 600 °C corresponds to the thermal degradation of MMT, which undergoes a dehydroxylation process. The TGA curves displayed in Fig. 5 clearly show that the exfoliated MMT acts as a barrier to the heat flow, hindering the different thermal degradation processes.

Table 3 summarizes the main electrochemical properties of nanometric PEDOT and PEDOT–MMT films. The charge

Table 3 Electrochemical properties of nanometric PEDOT and PEDOT–MMT films: charge storage (mC cm^{-2}), loss of electrostability (LES, in %; eqn (1)), specific capacitance determined by CV (SC, in F g^{-1}; eqn (4)), doping level (dl; eqn (2)), n_{ox} and n_{av} (both in electrons; eqn (3))

	Charge storage	LES	SC	dl	n_{ox}	n_{av}
PEDOT	26.1	15	355	0.49	2.05	1.56
PEDOT–MMT (5% w/w)	21.7	15	284	0.37	2.10	1.73
PEDOT–MMT (10% w/w)	20.3	16	265	0.33	2.15	1.82
PEDOT–MMT (20% w/w)	19.7	15	257	0.40	2.19	1.79
PEDOT–MMT (50% w/w)	18.1	16	237	0.37	2.20	1.83

storage decreases slowly but progressively when the concentration of clay increases. Specifically, the reduction in the charge storage of the nanocomposites with respect to pristine PEDOT ranges from 17% (MMT 5% w/w) to 30% (MMT 50% w/w). In contrast, the variation of the electrostability with the concentration of clay is negligible, LES values of the nanocomposites and PEDOT being practically identical (~15 to 16%). A similar behavior was observed for the charge storage of micrometric films (data not shown), the electrostability of these systems decreasing slightly with the concentration of clay (*e.g.* LES = 24% and 30% for micrometric PEDOT and PEDOT–MMT 20% w/w, respectively). This small variation was also observed in our previous work for composites with MMT ranging between 1% and 10% w/w.[34]

On the other hand, it should be emphasized that the SCs determined by CV (eqn (4)) for all the nanometric films are remarkably high (Table 3). Specifically, the SC of nanometric PEDOT is 355 F g^{-1}, which is one order of magnitude higher than that determined for the micrometric film (SC = 56 F g^{-1}). Although the SC of nanometric composites undergoes a reduction when the concentration of clay increases, their values are still considerably high, ranging from 284 F g^{-1} (MMT 5% w/w) to 237 F g^{-1} (MMT 50% w/w). The SC reported in the literature for micrometric PEDOT-inorganic hybrid nanocomposites involving MoO_3, RuO_2, carbon nanotubes, MnO_2, and $NiFe_2O_4$ varies between 153 and 375 F g^{-1},[42–48] evidencing the potential interest of nanometric films of both PEDOT and PEDOT–MMT films as electrochemical capacitors. In contrast, the SC of micrometric PEDOT–MMT films was lower than 106 F g^{-1} in all cases (*e.g.* SC = 96 F g^{-1} for micrometric PEDOT–MMT 20% w/w).

The doping levels (eqn (2)) determined for the PEDOT–MMT clays were found to be slightly lower than those of pristine PEDOT. The doping levels measured for nanometric films (Table 3) were similar to those obtained for the corresponding micrometric films in all cases (*e.g.* dl = 0.54 and 0.49 for micrometric and nanometric PEDOT, respectively). On the other hand, the degree of cross-linking is typically determined by the number of electrons consumed to incorporate a monomer into a polymer and to oxidize the resulting chain (n_{ox}), this information being determined through the electropolymerization kinetics (*i.e.* considering different polymerization times for the generation of polymer films under a constant potential).[52] After discounting the oxidation charge used to compensate the charge of the dopant ion of n_{ox}, the average number of electrons per monomer (n_{av}, where $n_{av} = n_{ox}$–dl) incorporated into a linear polymer chain obtained from a typical condensation mechanism should be $n_{av} = 2.0$ (*i.e.* two protons and two electrons are involved in the formation of the α–α bond between the terminal repeating unit of the polymer chain and the incorporated monomer).[59,60] Thus, undesired cross-linking reactions are probed when $n_{av} > 2.0$.

Table 3 includes the values of both n_{ox} and n_{av} for nanometric films of PEDOT and PEDOT–MMT. As it can be seen, n_{av} is lower than 2.0 in all cases. This feature indicates the existence of parallel chemical polymerization reactions based on proton transfer processes during the electrochemical polymerization. Accordingly, as no electron of the external circuit participates in such chemical processes, the resulting n_{av} values are lower than 2.0. However, the most noticeable result is that n_{av} is lower for PEDOT than for PEDOT–MMT, evidencing the protecting role exerted by the clay against parallel chemical processes. All these features, which are independent of the thickness of the film, were also identified in micrometric films.

Fabrication of type I ultracapacitors

Type I ultracapacitors are symmetric systems with the same p-dopable conducting polymer for the two electrodes. In this work symmetric PEDOT/PEDOT and PEDOT–MMT/PEDOT–MMT ultracapacitors were fabricated (Fig. 6a) using nanometric and micrometric films. The SC (eqn (4)) and the LES for 100 consecutive oxidation–reduction cycles (eqn (1)) of nanometric ultracapacitors are compared in Table 4. The SC of the ultracapacitor based on the symmetric assembly of two nanometric PEDOT films is 465 F g^{-1}, which represents a significant improvement with respect to the symmetric ultracapacitor prepared using micrometric PEDOT films (82 F g^{-1} in Table 4). Thus, the SC increases one order of magnitude when the thickness of the film is reduced from the micrometric (~1 μm) to the nanometric (~200 nm) scale.

The SC of nanometric PEDOT/PEDOT decreases by about one half when a MMT concentration ≤20% w/w is incorporated into the two films. Thus, nanometric PEDOT–MMT/PEDOT–MMT with MMT ≤ 20% w/w assemblies (identical MMT concentration in the two electrodes) show SC values ranging from 207 to 234 F g^{-1}. The drop of the SC is slightly higher for the assembly with MMT = 50% w/w (179 F g^{-1}). The detriment

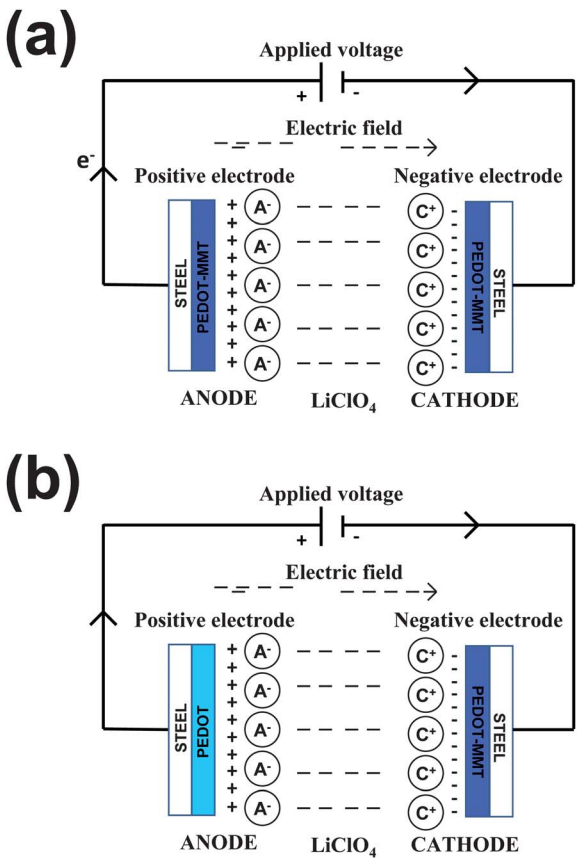

Fig. 6 Scheme of the (a) type I and (b) type II ultracapacitors.

Table 4 Performance of PEDOT and PEDOT–MMT electrodes in symmetric and asymmetric ultracapacitor configurations (Fig. 6). Results obtained for assemblies of both nanometric and micrometric films are displayed

Assembly	SC (CV)[a]	LES[b]	SC (EIS)[c]
Nanometric films			
PEDOT/PEDOT	465	35	—
PEDOT–MMT/PEDOT–MMT 5% w/w	217	41	—
PEDOT–MMT/PEDOT–MMT 10% w/w	207	39	—
PEDOT–MMT/PEDOT–MMT 20% w/w	234	40	—
PEDOT–MMT/PEDOT–MMT 50% w/w	179	38	—
PEDOT/PEDOT–MMT 20% w/w	429	37	386
Micrometric films			
PEDOT/PEDOT	82	21	64
PEDOT–MMT/PEDOT–MMT 20% w/w	94	35	75
PEDOT/PEDOT–MMT 20% w/w	116	43	88

[a] Specific capacitance determined by CV (eqn (4)), in F g^{-1}. [b] Loss of electroactivity (eqn (1)), in %. [c] Specific capacitance determined by EIS (eqn (8)), in F g^{-1}.

in the SC produced by the incorporation of MMT is fully consistent with the behavior discussed above for single electrode systems (Table 3). On the other hand, the LES values determined for clay-containing ultracapacitors are similar to that of the PEDOT/PEDOT one, evidencing that the influence of the MMT in the electrochemical stability is practically negligible at the nanometric scale. The electrostability determined for single electrode systems was higher than obtained for symmetric two electrodes assembled configurations, this feature being independent of the presence and concentration of clay. In spite of this, it should be emphasized that the electrochemical stability of the five symmetric ultracapacitors is significantly high, especially considering that LES values were determined using a large number of consecutive oxidation–reduction cycles.

Table 4 includes the SC and LES values determined by CV for micrometric PEDOT/PEDOT and PEDOT–MMT/PEDOT–MMT 20% w/w configurations, the latter being selected because this clay concentration provided the highest SC in the nanometric ultracapacitors. The SC of the ultracapacitor fabricated with the nanocomposite was slightly higher, even though the electrochemical stability of the PEDOT/PEDOT was greater. Moreover, the SC of the ultracapacitor fabricated using micrometric PEDOT was slightly higher than that measured for a single electrode, whereas the opposite tendency is observed for that prepared using the PEDOT–MMT 20% w/w.

The effect of the electrochemical degradation on the ultracapacitor behavior of micrometric PEDOT/PEDOT and PEDOT–MMT/PEDOT–MMT 20% w/w configurations was examined by comparing the SC, LES, P and E_{max} measured for samples as prepared and after 2000 consecutive oxidation–reduction cycles (Table 5). It should be mentioned that the SCs determined after 500 and 2000 consecutive oxidation–reduction cycles were similar (Fig. 7a), indicating that very small changes are expected for a larger number of cycles. A similar behavior was observed for LES, P and E_{max} (not shown). Results suggest that the positive effect of the clay in E_{max} disappears after such a number of oxidation–reduction cycles. In contrast, the power of the clay-containing symmetric ultracapacitor remains significantly higher than that of the PEDOT/PEDOT one after 2000 cycles, even though the relative difference between the two

Table 5 Influence of the electrochemical degradation in the specific capacitance, the power density, maximum specific energy and loss of electroactivity of PEDOT and PEDOT–MMT 20% w/w micrometric electrodes in symmetric and asymmetric ultracapacitor configurations

	SC[a]	SC[b]	P[c]	E_{max}[d]	LES[e]
PEDOT/PEDOT	82/37	77/64	1033/819	6.6/1.8	21/44/57
PEDOT–MMT/PEDOT–MMT 20% w/w	94/44	89/69	1465/1046	9.7/2.9	35/56/58
PEDOT/PEDOT–MMT 20% w/w	116/42	99/66	1682/1285	11.4/6.8	43/62/63

[a] Specific capacitance determined by CV (eqn (4)) for fresh samples/for samples after 2000 consecutive redox cycles, in F g^{-1}. [b] Specific capacitance derived from galvanostatic charge–discharge profiles (eqn (7)) for fresh samples/for samples after 1000 consecutive charge–discharge processes. [c] Power density determined from current charge–discharge cycles for fresh samples/for samples after 2000 consecutive redox cycles, (eqn (5)), in W kg^{-1}. [d] Maximum specific energy (eqn (6)) determined for fresh samples/for samples after 2000 consecutive redox cycles, in W h kg^{-1}. [e] Loss of electrostability (eqn (1)) after 100/500/2000 consecutive redox cycles, in %.

systems decreases from 42% to 29%. The relative electrochemical stabilities undergo some changes with the increase in the number of cycles, the PEDOT/PEDOT configuration being more electrostable than the PEDOT–MMT/PEDOT–MMT one by 14% and 1% after 100 and 2000 cycles, respectively. These features are

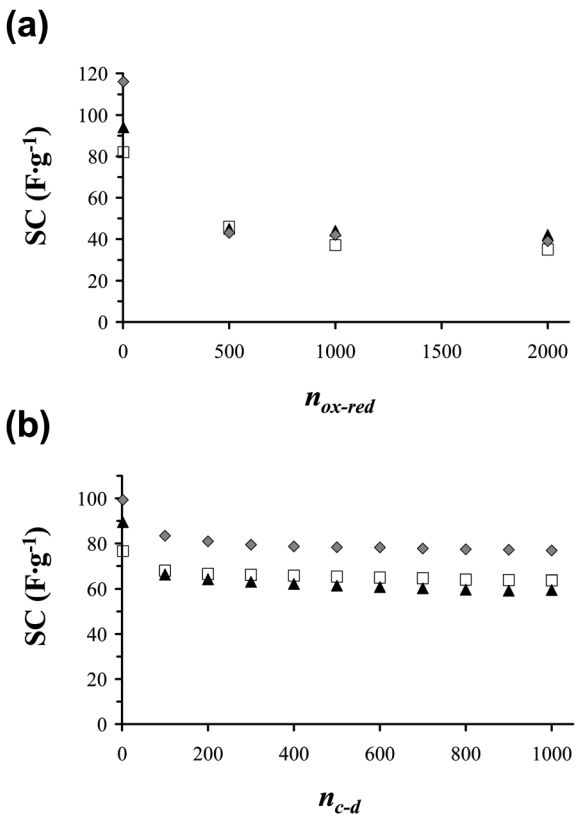

Fig. 7 Variation of the specific capacitance (SC) against (a) the number of consecutive oxidation–reduction cycles (n_{ox-red}) and (b) the number of charge–discharge cycles (n_{c-d}) for PEDOT/PEDOT (empty squares), PEDOT–MMT/PEDOT–MMT 20% w/w (black triangles) and PEDOT/PEDOT–MMT (grey diamonds).

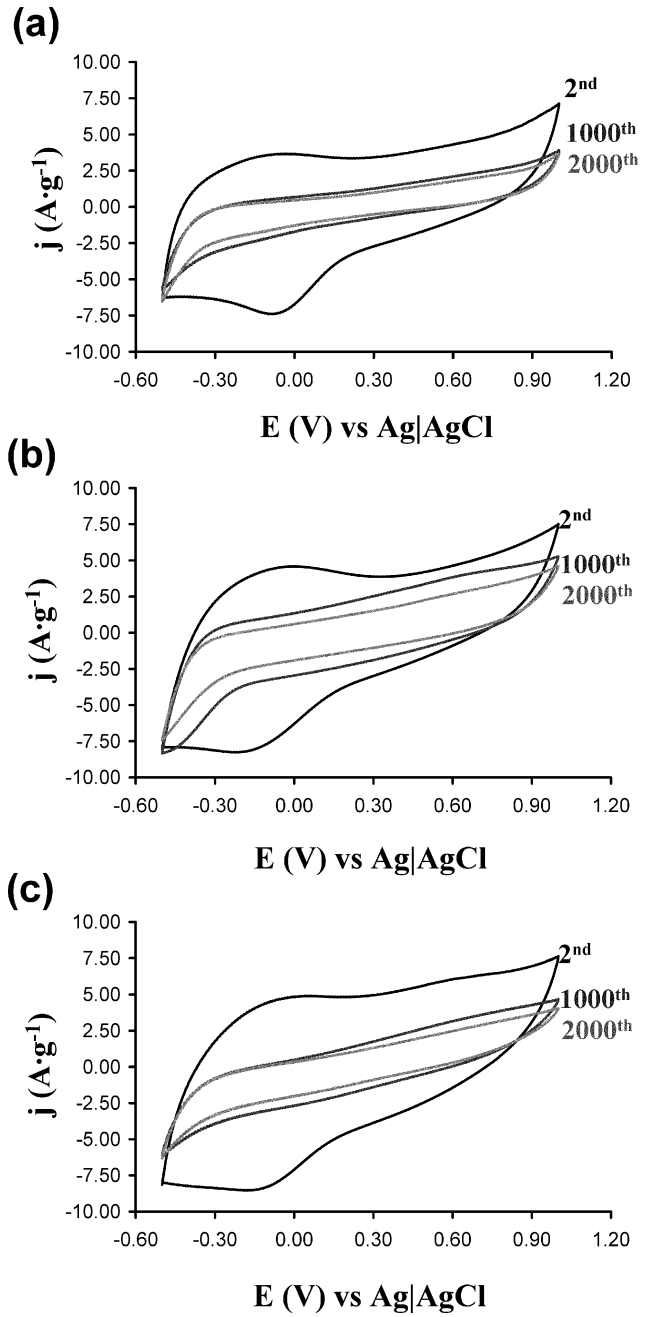

Fig. 8 Control voltammograms for 2, 1000 and 2000 consecutive oxidation–reduction cycles for (a) PEDOT/PEDOT; (b) PEDOT–MMT/PEDOT–MMT 20% w/w; and (c) PEDOT/PEDOT–MMT 20% w/w ultracapacitors. Voltammograms were recorded at 100 mV s^{-1}. Initial and final potentials: −0.50 V. Reversal potential: 1.00 V.

reflected in Fig. 8, which compares the cyclic voltammograms of PEDOT/PEDOT and PEDOT–MMT/PEDOT–MMT 20% w/w recorded after 2, 1000 and 2000 consecutive oxidation–reduction cycles.

The SCs determined by CV (eqn (4)) before and after 2000 consecutive oxidation–reduction cycles show decreases of 55% and 54% for PEDOT/PEDOT and PEDOT–MMT/PEDOT–MMT assemblies. These drastic reductions seem to suggest that the stability of two such capacitors is very low (*i.e.* SCs drop by

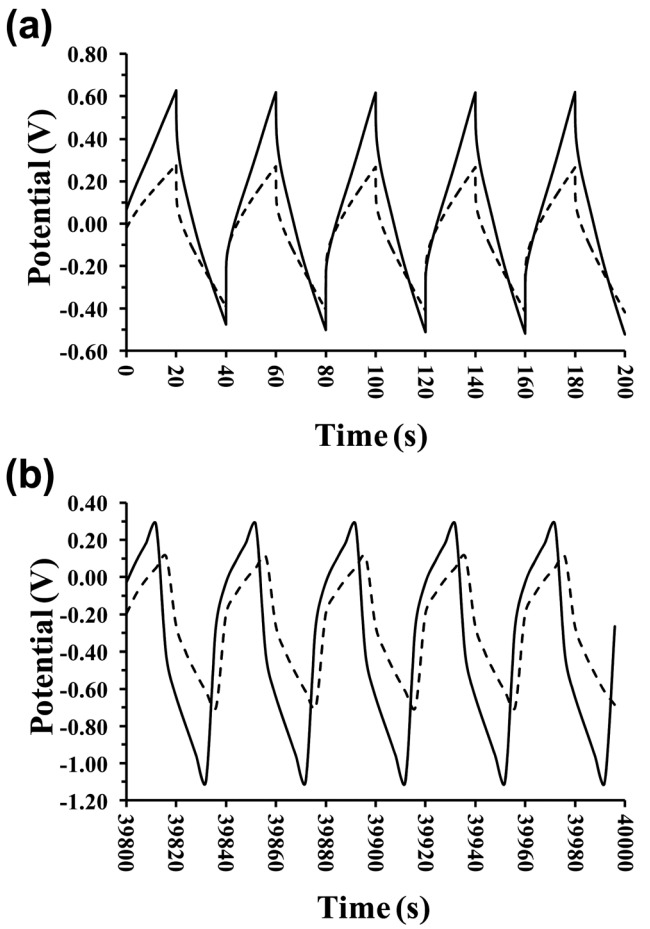

Fig. 9 Galvanostatic charge–discharge curves for PEDOT/PEDOT-MMT (solid line) and PEDOT-MMT/PEDOT-MMT (dashed line) ultracapacitors. From a total of 1000 charge–discharge cycles the (a) first and (b) last five cycles are displayed.

more than 50%). However, it should be emphasized that application of consecutive oxidation–reduction cycles is the most aggressive electrochemical method to determine the stability of the ultracapacitor behavior. In order to illustrate that the stability of PEDOT/PEDOT and PEDOT–MMT/PEDOT–MMT capacitors is relatively good, a less aggressive electrochemical method has been used. Charge and discharge profiles were linear and relatively symmetric in all cases (Fig. 9), which indicated the capacitive behavior of the two systems. The SCs of the two assemblies were re-evaluated using eqn (7) after applying one and 1000 galvanostatic charge–discharge processes, results being included in Table 5 and Fig. 7b. The SCs determined after one charge–discharge process (eqn (7)) are very similar to those obtained by CV (eqn (4)): the differences between the two procedures amounted to 5–6% only. However, after application of 1000 charge–discharge processes the SCs of PEDOT/PEDOT and PEDOT–MMT/PEDOT–MMT configurations drop 17% and 22% only. Indeed, the SCs remain practically unchanged after 100 cycles only (Fig. 7b).

Fabrication of type II ultracapacitors

Type II ultracapacitors correspond to asymmetric configurations based on two different conducting polymers with very different

electroactivities. In this work, micrometric and nanometric asymmetric systems have been fabricated by combining PEDOT and PEDOT–MMT 20% w/w electrodes in the same ultracapacitor (Fig. 6b). Results, which are included in Table 4, indicate that the SC and LES of nanometric PEDOT/PEDOT–MMT 20% w/w and PEDOT/PEDOT are very similar. The performance of the former asymmetric assembly is considerably better than that of symmetric PEDOT–MMT/PEDOT–MMT in terms of both capacitance and electrochemical stability. This represents a significant advance since the combination of nanometric thickness with the use of an exfoliated MMT-containing electrode allows the fabrication of thermally stable advanced ultracapacitors. Indeed, the SC measured for nanometric PEDOT/PEDOT–MMT 20% w/w is higher than those determined for conventional nanocomposites of PEDOT and inorganic materials.[42–48] On the other hand, the SC of micrometric PEDOT/PEDOT–MMT 20% w/w is 41% and 23% higher than those of symmetric PEDOT and PEDOT–MMT/PEDOT–MMT 20% w/w, respectively. This feature corroborates that the incorporation of the exfoliated clay produces a very significant benefit in asymmetric ultracapacitors, independently of the thickness of the films.

The effect of electrochemical degradation on the ultracapacitor behavior of micrometric PEDOT/PEDOT–MMT 20% w/w is included in Table 5 and Fig. 7. Results clearly indicate that the impact of 2000 consecutive oxidation–reduction cycles in the SC and LES (Fig. 7 and 8) of the type II ultracapacitor is similar to that discussed above for the type I ones. However, reduction of the SC after application of 1000 galvanostatic charge–discharge processes is relatively low (*i.e.* the SC drops 63% and 64% after 500 and 2000 consecutive oxidation–reduction cycles, respectively, and 33% after 1000 consecutive charge–discharge processes). Moreover, as occurred for the type I ultracapacitors, the SC essentially drops during the first 100 charge–discharge cycles, remaining practically unaltered for the next 900 cycles (Fig. 7b). Results displayed in Table 5 reflect that the influence of the electrochemical degradation is less important for the asymmetric configuration than for the symmetric one. Thus, the positive effect of the clay in P and E_{max} is retained after such a number of cycles. For example, the power of the type II ultracapacitor is 217 and 239 W kg^{-1} higher than that of the type I one for the device as prepared and after 2000 cycles, respectively. A very similar behavior is detected for E_{max}, which is higher for the PEDOT/PEDOT–MMT ultracapacitor than for the PEDOT–MMT/PEDOT–MMT and PEDOT/PEDOT ones.

Electrochemical impedances spectroscopy studies of type I and type II ultracapacitors

Fig. 10 shows the EIS spectra of micrometric PEDOT/PEDOT (Fig. 10a), PEDOT–MMT/PEDOT–MMT 20% w/w (Fig. 10b) and PEDOT/PEDOT–MMT 20% w/w (Fig. 10c) ultracapacitors as prepared and after 500 consecutive oxidation–reduction cycles. The spectra were fitted using an equivalent circuit (EC). The aim of the choice of the EC was to obtain a satisfactory fitting of the experimental data, where the circuit elements can be associated with the physical phenomena that are probably taking place at the electrode surface. The EC proposed was $R_s(CPE_1[R_{CT}W])C_{PS}$ (Fig. 10d), where R_s represents the electrolyte resistance, CPE_1 the double layer capacitance, R_{CT} the

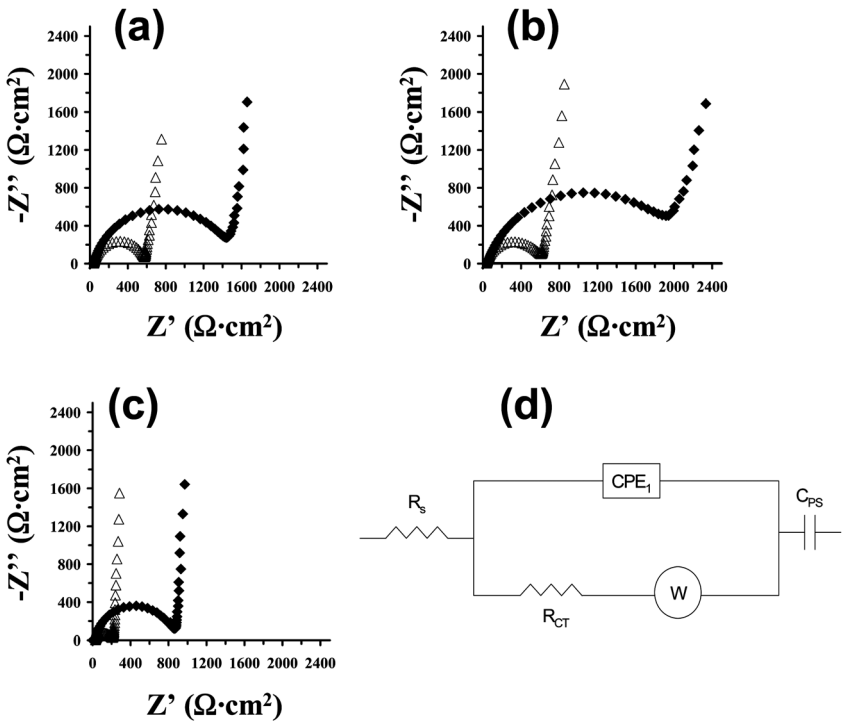

Fig. 10 Nyquist plots showing the evolution of the impedance data of micrometric ultracapacitors as prepared (empty triangles) and after 500 consecutive oxidation–reduction cycles (filled diamonds): (a) PEDOT/PEDOT; (b) PEDOT–MMT/PEDOT–MMT 20% w/w; and (c) PEDOT/PEDOT–MMT 20% w/w. Experimental data (represented symbols) were fitted to the equivalent circuit model depicted in (d) to produce the parameters listed in Table 6.

charge-transfer resistance at the polymer film–electrolyte interface, which is in serial connection with the Warburg element (W), and C_{PS} the faradaic pseudo-capacitance corresponding to a practically vertical line at low frequency region of the EIS spectra. The double layer capacitance was replaced by a constant phase element (CPE) that describes a non-ideal capacitor when the phase angle is different from −90°. The CPE impedance has been expressed as:

$$Z_{CPE} = [Q(j\omega)^n]^{-1} \quad (9)$$

The CPE represents a capacitor and a resistor for $n = 1$ and $n = 0$, respectively, while it is associated with a diffusion process when $n = 0.5$. The CPE impedance is attributed to the distributed surface reactivity, surface heterogeneity, and roughness of the current and potential distribution, which in turn are related to the electrode geometry and the electrode porosity.[61] The Warburg impedance was included taking into account the diffusion phenomena.[62] The quality of fitting was evaluated using the error percentage associated to each circuit component, errors smaller than 5% being obtained in all cases.

Table 6 lists the parameters derived from the fitting of the EIS plots displayed in Fig. 10a–c to the EC previously described. R_{CT} increases with the number of oxidation–reduction cycles in all cases. The highest R_{CT} value was obtained for the symmetric PEDOT–MMT/PEDOT–MMT configuration, independently of the number of cycles. This has been attributed to the barrier effect induced by the microscopic structure of nanocomposite: the exfoliated clay hinders the entrance of perchlorate ions, increasing the ionic charge-transfer resistance. This behavior is fully consistent with the electrostability of PEDOT–MMT/PEDOT–MMT, which is lower than that of PEDOT/PEDOT (Table 4).

The CPE impedance is higher for PEDOT–MMT/PEDOT–MMT than for PEDOT/PEDOT, indicating that the effective surface area for interfacial charge transport is highest for the PEDOT–MMT than for PEDOT. This observation suggests that the presence of pores and cavities is higher in the former than in the latter, which is fully consistent with the SEM micrographs displayed in Fig. 3a and b. On the other hand, Table 6 shows that the Warburg impedance decreases after 500 oxidation–reduction cycles. This feature has been attributed to the fact that the degradation of the polymer increases with the number of cycles. More specifically, electrochemical degradation produces structural changes on the surface of the polymer. Fig. 11a and b show SEM micrographs of micrometric PEDOT and PEDOT–MMT 20%, respectively, after 500 oxidation–reduction cycles. Comparison with the morphology of fresh samples, which are displayed in Fig. 2a and b, evidences that electrochemical degradation produce deep cracks on the surface (Fig. 11c), which facilitate the diffusion process. This phenomenon has been attributed to the fact that clusters of aggregated molecules tend to collapse when the samples are submitted to a large number of oxidation–reduction cycles.[18] In other words, the homogeneous distribution of small pores and cavities transforms into well localized cracks upon such collapses.

The asymmetric PEDOT/PEDOT–MMT configuration presents the lowest R_{CT} value, which is consistent with its highest SC. This indicates that the diffusion of perchlorate ions is easier than in the two type I ultracapacitors. In spite of this, the electrochemical stability of the asymmetric ultracapacitor was found to

Table 6 Fitting parameters used to simulate the EIS data obtained for the micrometric ultracapacitors studied in this work (Fig. 10)

	R_s[a]	CPE_1[b]	n_1[c]	R_{CT}[d]	W[e]	C_{PS}[f]
As prepared						
PEDOT/PEDOT	40.82	49.57	0.88	537.23	10.08	13.22
PEDOT–MMT/PEDOT–MMT	38.61	62.95	0.85	568.82	14.66	9.42
PEDOT/PEDOT–MMT	29.55	9.82	0.87	178.18	25.41	10.95
After 500 consecutive oxidation–reduction cycles						
PEDOT/PEDOT	36.56	10.85	0.81	1488.15	2.61	9.75
PEDOT–MMT/PEDOT–MMT	41.44	10.44	0.77	2064.42	5.02	10.92
PEDOT/PEDOT–MMT	31.01	12.34	0.87	592.73	13.59	2.92

[a] Electrolyte resistance, in Ω cm². [b] Double layer capacitance, in μF cm^{-2} s^{n-1}. [c] From eqn (9). [d] Charge-transfer resistance at the polymer film–electrolyte interface, in Ω cm². [e] Warburg element, in Ω cm². [f] Faradaic pseudo-capacitance, in mF cm^{-2}.

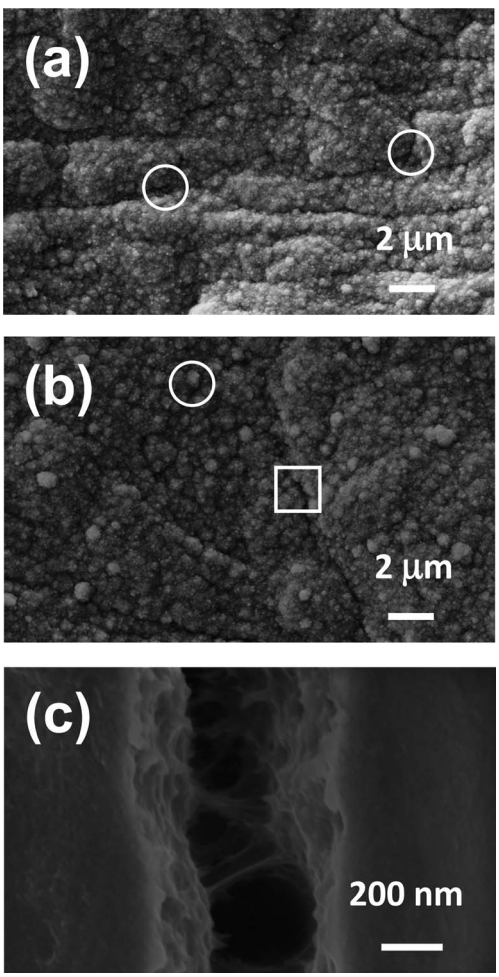

Fig. 11 SEM micrographs of micrometric (a) PEDOT and (b) PEDOT–MMT 20% w/w after 500 consecutive oxidation–reduction cycles. The white circles and the white square illustrate the deep cracks produced by the electrochemical degradation. (c) High resolution SEM micrograph of the crack marked with a white square in (b).

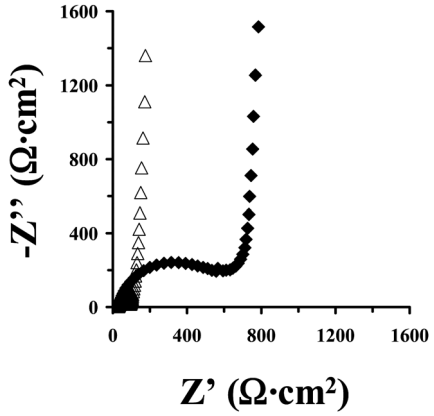

Fig. 12 Nyquist plots showing the evolution of the impedance data of the nanometric PEDOT/PEDOT–MMT 20% w/w ultracapacitor as prepared (empty triangles) and after 500 consecutive oxidation–reduction cycles (filled diamonds). The experimental data (represented symbols) were fitted to the equivalent circuit model depicted in Fig. 10d to produce the parameters listed in Table 7.

Table 7 Fitting parameters used to simulate the EIS data obtained for the nanometric PEDOT/PEDOT–MMT 20% w/w ultracapacitor (Fig. 12)

	R_s[a]	CPE_1[b]	n_1[c]	R_{CT}[d]	W[e]	C_{PS}[f]
As prepared	30.90	8.34	0.86	62.14	59.58	3.08
After 500 consecutive oxidation–reduction cycles	31.01	12.34	0.87	592.27	13.59	2.92

[a] Electrolyte resistance, in Ω cm². [b] Double layer capacitance, in μF cm^{-2} s^{n-1}. [c] From eqn (9). [d] Charge-transfer resistance at the polymer film–electrolyte interface, in Ω cm². [e] Warburg element, in Ω cm². [f] Faradaic pseudo-capacitance, in mF cm^{-2}.

be lower than that of the symmetric ones. Understanding of this apparent contradiction is provided in Table 6. Thus, the low electrostability of the PEDOT/PEDOT–MMT ultracapacitor should be attributed to the high Warburg impedance reached after 500 redox cycles.

The nanometric PEDOT/PEDOT–MMT 20% w/w is the only ultracapacitor made of ultrathin films studied in this work. This system has been selected because its SC is two times higher than the SCs determined for all the nanometric symmetric configurations (Table 4). Fig. 12 shows the EIS plots of the nanometric PEDOT/PEDOT–MMT 20% w/w as prepared and after 500 consecutive oxidation–reduction cycles, and Table 7 lists the parameters derived from their fitting to the EC displayed in Fig. 10d. This nanometric ultracapacitor follows the same behavior as the corresponding micrometric one, even though the values found for the different elements of the EC were smaller for the former than for the latter. R_{CT} increases with the number of oxidation–reduction cycles, while the Warburg impedance decreases. Moreover, electrochemical degradation of the nanometric films produces deep cracks on the surface similar to those displayed in Fig. 11 for micrometric films.

Finally, the SCs provided by EIS (eqn (8)) for the investigated ultracapacitors are included in Table 4. These values are fully consistent with those derived from CV. For micrometric devices the two methodologies indicate that the lowest SC corresponds to the PEDOT/PEDOT, whereas the asymmetric PEDOT/PEDOT–MMT 20% w/w shows the highest one. In spite of this, the values determined by EIS are underestimated by 20–24% with respect to those measured using CV. Such overestimation decreases to 10% for the nanometric PEDOT/PEDOT–MMT 20% w/w, the SCs measured by EIS and CV being 386 and 429 F g^{-1}, respectively.

Conclusions

Exfoliated PEDOT–MMT nanocomposites have been prepared by anodic polymerization considering MMT concentrations in the generation medium ranging from 5% w/w to 50% w/w. Nanometric and micrometric films, with a thickness of ~200 nm and ~1 μm, respectively, have been obtained by controlling the polymerization time. SEM and AFM analyses indicate that low concentrations of MMT (≤10% w/w) induce changes in the morphology of the internal side of the film only. Specifically, the precipitation of the clay on the electrode provokes a homogeneous distribution of granules in the internal surface. In contrast, MMT concentrations ≥ 20% w/w produce the formation of large aggregates in the surface of the external side of the film and thin cracks in the internal side, the latter being due to the swelling effect promoted by the absorbed water.

The electrical conductivity decreases one order of magnitude upon the incorporation of a concentration of MMT ≥ 20% w/w. The adherence and thermal stability are lower for PEDOT than for the nanocomposites, increasing moderately with the concentration of MMT. In contrast both the charge storage and dl decreases when the concentration of clay increases. The SC and electrostability largely depend on the thickness of the films. Thus, the SCs of nanometric PEDOT and PEDOT–MMT, which range from 355 to 237 F g^{-1} (PEDOT and PEDOT–MMT 50% w/w, respectively), are one order of magnitude higher than those of the corresponding micrometric films. Similarly, the electrostability of micrometric PEDOT–MMT films is lower than that of nanometric ones.

Nanometric ultracapacitors of types I and II (*i.e.* symmetric and asymmetric configurations of two electrodes) show very high SC values. The larger SC corresponds to the symmetric PEDOT/PEDOT and the asymmetric PEDOT/PEDOT–MMT 20% w/w (465 and 429 F g^{-1}, respectively), whereas the SC of PEDOT–MMT/PEDOT–MMT decreases from 217 to 179 F g^{-1} when concentration of MMT increases from 5% to 50% w/w. In contrast, the clay does not alter the electrostability of these nanometric ultracapacitors, the LES of nanometric ultracapacitors being very similar independently of their symmetric or asymmetric configurations. On the other hand, the SCs of micrometric PEDOT–MMT/PEDOT–MMT 20% w/w and PEDOT/PEDOT–MMT 20% w/w are higher than that of PEDOT/PEDOT, even though the latter shows the highest electrochemical stability. The capabilities and properties of the micrometric ultracapacitors as well as of the nanometric PEDOT/PEDOT–MMT 20% w/w have been rationalized using EIS assays.

Electrochemical degradation studies using consecutive oxidation–reduction cycles indicate that the favorable effect of the clay on the SC and electrochemical stability of both type I and II

ultracapacitors decreases significantly after 500 consecutive oxidation–reduction cycles. This effect is much less pronounced when electrochemical degradation is carried out using charge–discharge cycles. In this case, the reduction of the SC is relatively low and, in addition, the asymmetric configuration retains the favorable effect of the clay on the SC, the power density and the maximum specific energy. On the other hand, EIS and SEM studies indicate that the electrochemical degradation produces deep cracks on the surface of the films, facilitating the diffusion of ions.

Acknowledgements

This work has been supported by MICINN and FEDER funds (MAT2009-09138 and MAT2009-11503), by the International Cooperation Program from Brazilian and Spanish Education Ministries CAPES-MICINN (PHB2007-0038-PC), and by the DIUE of the Generalitat de Catalunya (contract numbers 2009SGR925 and 2009SGR1208). Support for the research of C.A. was received through the prize "ICREA Academia" for excellence in research funded by the Generalitat de Catalunya. D.A. is thanked for the financial support through a FPI-UPC grant.

References

1 F. Jonas and L. Schrader, *Synth. Met.*, 1991, **41**, 831.
2 M. Dietrich, J. Heinze, G. Heywang and F. Jonas, *J. Electroanal. Chem.*, 1994, **369**, 87.
3 G. Heywang and F. Jonas, *Adv. Mater.*, 1992, **4**, 116.
4 L. Groenendaal, F. Jonas, D. Freitag, H. Pielartzik and J. R. Reynolds, *Adv. Mater.*, 2000, **12**, 481.
5 Q. Pei, G. Zuccarello, M. Ahlskog and O. Ingana, *Polymer*, 1994, **35**, 1437.
6 A. G. Bayer, *Euro Pat.*, 339340, 1988.
7 J. Apperloo, L. B. Groenendaal, H. Verheyen, M. Jayakannan, R. A. Janssen, A. Dkhissi, D. Beljonne, R. Lazzaroni and J. L. Brédas, *Chem.–Eur. J.*, 2002, **8**, 2384.
8 J. Yu and S. Holdcroft, *Chem. Mater.*, 2002, **14**, 3705.
9 B. Sankaran and J. R. Reynolds, *Macromolecules*, 1997, **30**, 2582.
10 J. Casanovas and C. Alemán, *J. Phys. Chem. C*, 2007, **111**, 4823.
11 J. Poater, J. Casanovas, M. Solà and C. Alemán, *J. Phys. Chem. A*, 2010, **114**, 1023.
12 W. Craft, F. Jonas, B. Muys and D. Qintens, (AgfaGevaert), Euro Pat., 564911, 1993.
13 T. Soboleva, Z. Xie, Z. Shi, E. Tsang, T. Navessin and S. Holdcroft, *J. Electroanal. Chem.*, 2008, **622**, 145.
14 D. M. de Leeuw, P. A. Kraakman, P. F. G. Bongaerts and C. M. J. Mutsaers, *Synth. Met.*, 1994, **66**, 263.
15 W. H. Heuer, R. Wehrmann and S. Kirchmayer, *Adv. Funct. Mater.*, 2002, **12**, 89.
16 C. A. Cutler, M. Bouguettaya and J. R. Reynolds, *Adv. Mater.*, 2002, **14**, 684.
17 S. Ghosh and O. Inganas, *Adv. Mater.*, 1999, **11**, 1214.
18 D. Aradilla, F. Estrany and C. Alemán, *J. Phys. Chem. C*, 2011, **115**, 8430.
19 S. Kirchmeyer and K. Reuter, *J. Mater. Chem.*, 2005, **15**, 2077.
20 P. Novak, K. Muller, K. S. V. Santhanam and O. Haas, *Chem. Rev.*, 1997, **97**, 207.
21 P. Aranda, M. Darder, R. Fernández-Saavedra, M. López-Blanco and E. Ruiz-Hitzky, *Thin Solid Films*, 2006, **495**, 104.
22 Rajesh, T. Ahuja and D. Kumar, *Sens. Actuators, B*, 2009, **136**, 275.
23 J.-M. Yeh and K.-C. Chang, *J. Ind. Eng. Chem.*, 2008, **14**, 275.
24 A. Olad and A. Rashidzadeh, *Prog. Org. Coat.*, 2008, **62**, 293.
25 J.-M. Yeh, S.-J. Liou, C.-Y. Lai and P.-C. Wu, *Chem. Mater.*, 2001, **13**, 1131.
26 W. Jia, E. Segal, D. Kornemandel, Y. Lamhot, M. Narkis and A. Siegmann, *Synth. Met.*, 2002, **128**, 115.
27 B.-H. Kim, J.-H. Jung, S.-H. Hong and J. Joo, *Macromolecules*, 2002, **35**, 1419.
28 W. J. Bae, K.-H. Kim, W. H. Jo and Y. H. Park, *Macromolecules*, 2004, **37**, 9850.
29 M. R. Karim and J. H. Yeum, *J. Polym. Sci., Part B: Polym. Phys.*, 2008, **46**, 2279.
30 K. Suri, S. Annapoorni, R. P. Tandom and N. C. Mehra, *Synth. Met.*, 2002, **126**, 137.
31 S. Leta, P. Aranda, R. Fernández-Saavedra Margeson, C. Detelliera and E. Ruiz- Hitzky, *J. Mater. Chem.*, 2008, **18**, 2227.
32 R. M. G. Rajapakse, S. Higgins, K. Velauthamurthy, H. M. N. Bandara, S. Wijeratne and R. M. M. Y. J. Rajapakse, *J. Compos. Mater.*, 2010, **45**, 597.
33 Y. Han and Y. Lu, *J. Appl. Polym. Sci.*, 2009, **11**, 2400.
34 D. Aradilla, F. Estrany, D. S. Azambuja, M. T. Casas, J. Puiggalí, C. A. Ferreira and C. Alemán, *Eur. Polym. J.*, 2010, **46**, 977.
35 W. J. Bae, K. H. Kim, Y. H. Park and W. H. Jo, *Macromolecules*, 2004, **37**, 9850.
36 R. Kotz and M. Carlen, *Electrochim. Acta*, 2000, **45**, 2483.
37 E. Frackowiak and F. Beguin, *Carbon*, 2002, **40**, 1775.
38 Y. G. Wang and X. G. Zhang, *Electrochim. Acta*, 2004, **49**, 1957.
39 C. Liu, F. Li, L.-P. Ma and H.-M. Cheng, *Adv. Mater.*, 2010, **22**, E28.
40 G. Centi and S. Perathoner, *Eur. J. Inorg. Chem.*, 2009, **26**, 3851.
41 G. A. Snook, P. Kao and A. Best, *J. Power Sources*, 2011, **196**, 1.
42 L. Chen, C. Yuan, H. Dou, B. Gao, S. Chen and X. Zhang, *Electrochim. Acta*, 2009, **54**, 2335.
43 A. V. Murugan, A. K. Viswanath, G. Gampet, C. S. Gopinath and K. Vijayamohanan, *Appl. Phys. Lett.*, 2005, **87**, 243511.
44 R. Sharma and L. Zhai, *Electrochim. Acta*, 2009, **54**, 7148.
45 P. M. Sen and M. De, *Electrochim. Acta*, 2010, **55**, 4677.
46 B. Banafsheh and D. G. Ivey, *Electrochim. Acta*, 2010, **55**, 2014.
47 L. Chen, C. Yuan, B. Gao, S. Chen and X. Zhang, *J. Solid State Electrochem.*, 2009, **13**, 1925.
48 A. V. Murugan, A. K. Viswanath, C. S. Gopinath and K. Vijayamohanan, *J. Appl. Phys.*, 2006, **100**, 074319.
49 F. Estrany, D. Aradilla, R. Oliver and C. Alemán, *Eur. Polym. J.*, 2007, **43**, 1876.
50 F. Estrany, D. Aradilla, R. Oliver, E. Armelin and C. Alemán, *Eur. Polym. J.*, 2008, **44**, 1323.
51 J. Carrasco, E. Brillas, V. Fernández, P. L. Cabot, J. A. Garrido, F. Centellas and R. M. Rodríguez, *J. Electrochem. Soc.*, 2001, **148**, E19.
52 R. Oliver, A. Muñoz, C. Ocampo, C. Alemán, E. Armelin and F. Estrany, *Chem. Phys.*, 2006, **328**, 299.
53 C. Ocampo, R. Oliver, E. Armelin, C. Alemán and F. Estrany, *J. Polym. Res.*, 2006, **13**, 193.
54 J. Madejová, B. Arvaiová and P. Komadel, *Spectrochim. Acta, Part A*, 1999, **55**, 2467.
55 D. Aradilla, F. Estrany, E. Armelin and C. Alemán, *Thin Solid Films*, 2010, **518**, 4203.
56 K. H. Hsieh, K. S. Ho, Y. Z. Wang, S. D. Ko and S. C. Fu, *Synth. Met.*, 2001, **123**, 217.
57 O. Bertran, E. Armelin, F. Estrany, A. Gomes, J. Torras and C. Alemán, *J. Phys. Chem. B*, 2010, **114**, 6281.
58 X.-G. Li, J. Li and M.-R. Huang, *Chem.–Eur. J.*, 2009, **15**, 6446.
59 E. M. Geneis, G. Bidan and A. F. Diaz, *J. Electroanal. Chem.*, 1983, **149**, 101.
60 V. S. Vashanta and K. L. N. Phani, *J. Electroanal. Chem.*, 2002, **520**, 79.
61 J.-B. Jorcin, M. E. Orazen, N. Pébère and B. Tribollet, *Electrochim. Acta*, 2006, **51**, 1473.
62 G. W. Walter, *Corros. Sci.*, 1986, **26**, 681.

